



# Investigation of film solidification and binder migration during drying of Li-Ion battery anodes



Stefan Jaiser<sup>a,\*</sup>, Marcus Müller<sup>b</sup>, Michael Baunach<sup>a</sup>, Werner Bauer<sup>b</sup>, Philip Scharfer<sup>a</sup>, Wilhelm Schabel<sup>a</sup>

<sup>a</sup> Institute of Thermal Process Engineering – Thin Film Technology, Karlsruhe Institute of Technology, Kaiserstraße 12, D-76131 Karlsruhe, Germany

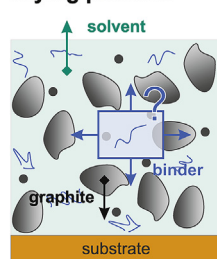
<sup>b</sup> Institute for Applied Materials – Ceramic Materials and Technologies, Karlsruhe Institute of Technology, Hermann-von-Helmholtzplatz 1, D-76344 Eggenstein-Leopoldshafen, Germany

## HIGHLIGHTS

- Insight into the property-determining drying and solidification of electrode films.
- Characteristic drying stages are revealed by a new experimental approach.
- High drying rates trigger binder gradients throughout electrode films.
- A top-down consolidation mechanism based on capillarity and diffusion is proposed.
- The impact of drying rate on electrochemical properties is revealed.

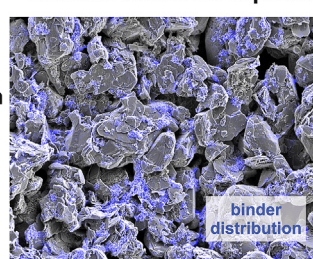
## GRAPHICAL ABSTRACT

### Drying process



film  
solidification

### Microstructure & Properties



## ARTICLE INFO

### Article history:

Received 27 January 2016

Received in revised form

26 March 2016

Accepted 3 April 2016

Available online 12 April 2016

### Keywords:

Binder migration

Film solidification

Drying

Adhesion

Energy-dispersive x-ray spectroscopy

Lithium-ion battery

## ABSTRACT

The property determining micro-structure of battery electrodes essentially evolves during drying, appointing it a paramount, yet insufficiently understood processing step in cell manufacturing. The distribution of functional additives such as binder or carbon black throughout the film strongly depends on the drying process. A representative state-of-the-art model system comprising graphite, polymeric binder, carbon black and solvent is investigated to gain an insight into the underlying processes. A new experimental approach is introduced that allows for revelation of the evolution of binder concentration gradients throughout the film during drying. Binder is detected by means of energy-dispersive x-ray spectroscopy (EDS) at the top and bottom surface. Drying kinetics is investigated and the impact of the drying process on electrochemical performance is disclosed. The enrichment of binder at the surface, which is observed while applying high drying rates, is shown to depend on two fundamental processes, namely capillary action and diffusion. The findings reveal characteristic drying stages that provide fundamental insights into film solidification. Based on that, a top-down consolidation mechanism capable of explaining the experimental findings is disclosed. Adhesion of the active layer to the substrate is shown to strongly depend on the local binder concentration in the vicinity of the substrate.

© 2016 Elsevier B.V. All rights reserved.

\* Corresponding author.

E-mail addresses: [stefan.jaiser@kit.edu](mailto:stefan.jaiser@kit.edu) (S. Jaiser), [marcus.mueller@kit.edu](mailto:marcus.mueller@kit.edu) (M. Müller), [michael.baunach@kit.edu](mailto:michael.baunach@kit.edu) (M. Baunach), [werner.bauer@kit.edu](mailto:werner.bauer@kit.edu) (W. Bauer), [philip.scharfer@kit.edu](mailto:philip.scharfer@kit.edu) (P. Scharfer), [wilhelm.schabel@kit.edu](mailto:wilhelm.schabel@kit.edu) (W. Schabel).

## 1. Introduction

Thin, functional films produced through coating and drying of particulate dispersions are widely spread in a plurality of

applications such as paper coatings [1–3], latex films [4–6] or lithium-ion battery electrodes [7,8]. The latter has been intensely discussed in recent years in particular and many improvements have been achieved, for instance by the introduction of new active materials or binder systems [9,10]. It is widely accepted in all of these applications that the process steps required for film production in general and the drying in particular are of paramount importance for film properties, which are governed by the film's internal structure or morphology [1,11–14].

Against this background it is quite remarkable, that only few publications in the field of battery coatings are addressing the complex interrelations of processing and film properties. While the effect of mixing [15–19] and the mixing tool [15,20] are at least somewhat reviewed, the coating [21,22] and drying [7,8,11,12,23] steps are hardly discussed. Likewise, the calendaring is only focused on in few publications [24,25]. One reason may be the extent of process control along the whole process chain from mixing to calendaring, which is an essential requirement for granting reproducible investigations into a single process step [26]. As a matter of course, this is also true for the evaluation and introduction of new battery materials.

Two driving forces prevail in research on lithium-ion battery electrodes: Cost reduction and improvements in energy density. The latter objective is mainly addressed in research on new materials. But especially the manufacturing has great potential to contribute to the aspired progress. The electrode film comprises active material particles and additives like disperse or soluble binder and conductivity-enhancing nanoparticles such as carbon black. An optimized electrode microstructure features a maximized active material content and a functional distribution of additives. A fundamental understanding of the governing processes occurring during electrode manufacturing and their impact on component distribution can therefore contribute to the establishment of improved mixing, coating, drying or calendaring processes.

Regarding the manufacturing costs, an increase in throughput would be desirable. At present, the drying process constitutes the major bottleneck in production speed. An increase in production speed is inevitably linked to an amplification of dryer capacity and therefore investment costs. The promotion of a better understanding of the governing processes occurring through the various stages during drying is obligatory to increase the potential of state-of-the-art dryers by engineering customized drying profiles.

The evolution of the electrode's micro-structure occurs exceedingly during drying [6–8,23]. As mentioned above, publications on the drying step are scarce with respect to lithium-ion battery material systems. Consequently, film solidification and mechanisms that influence film structure are hardly discussed. On the contrary, paper and latex coatings have been subjected to intensive research in the past decades, which has resulted in a fairly sound understanding of film solidification and the mechanisms affecting film properties [6,27–33]. Although some major differences become obvious when comparing both applications, the findings might nevertheless be adopted and could possibly form the basis for models that describe film solidification in battery electrode films and drying dispersions in general. This hypothesis is supported by analogies found regarding the binder migration, which was observed previously in publications on coated paper [2,29], latex [6,33] as well as in battery electrode drying [7,8,23].

This work illuminates the underlying processes occurring during solvent removal that significantly govern the final film properties. A new experimental approach is developed for this purpose. The basic concept comprises the consecutive adjustment of a high (HDR) and a low drying rate (LDR) in a single isothermal drying step and the assessment and comparison of

anode films produced under variation of the transition between the two drying rates that therefore exhibit different drying histories. The approach exploits the stronger extent to which binder migration occurs under harsh drying conditions [8] and, thus, allows for identification of the evolution of binder concentration gradients throughout the film. The experiments are conducted under well-defined boundary conditions that allow for interpretation of the drying kinetics. The evolution of binder gradients is evaluated on the basis of the binder concentration at the free surface and the interface between the active layer and the substrate after delamination by means of energy-dispersive x-ray spectroscopy (EDS). In addition, adhesive force to the substrate is introduced as indirect measure for the local binder concentration in the vicinity of the substrate. The findings provide an insight into the fundamental solidification mechanism of anode films. As a result, a model based on capillarity and diffusion is presented that describes film formation and component distribution depending on the drying boundary conditions. Electrochemical tests of selected anode films are presented, which underline the important role of the drying process in terms of electrode quality.

## 2. Experimental

### 2.1. Mixing

After dry pre-blending of commercial graphite (SMG-A, Hitachi Chemicals, Japan,  $d_{50} = 20.4 \mu\text{m}$ ) and carbon black (C-ENERGY C65,  $d_{50} = 65 \text{ nm}$ , Imerys Graphite & Carbon, Bodio, Switzerland), the binder solution comprising Polyvinylidene fluoride (PVDF; Solvay Solef 5130, Brussels, Belgium) and *N*-Methyl-2-pyrrolidone (NMP; Carl Roth) was added stepwise at a polymer mass fraction of 5.55% to reduce carbon black agglomeration, thereby following the recommendations given by Terashita and Miyamoto [34] and Lee et al. [16]. At the final solid content the slurry was homogenized and degassed under vacuum. The mixing process was conducted in a laboratory dissolver equipped with a custom-built mixing tool enhancing vertical transport. A more detailed description of the mixing procedure is provided in the [supporting information](#). The composition of the final dispersion and the dry films are listed in [Table 1](#).

### 2.2. Coating

Both coating and drying were conducted in a custom-built setup comprising an impingement dryer and a temperature-controlled aluminum plate ([Fig. 1](#)).

Films 60 mm wide and 80 cm long were applied on 10  $\mu\text{m}$  copper foil (Nippon Foil Mfg. Co. Ltd., Tokyo, Japan) by knife coating at a speed of 10  $\text{cm s}^{-1}$ . Both dryer and aluminum plate were operated at a constant temperature of 76.5 °C. The doctor blade as well as anode slurry were pre-heated to the same temperature prior to film application. The mean area loading of the dry films and the average dry film thickness were  $70.5 \pm 1.7 \text{ g m}^{-2}$  and about 78  $\mu\text{m}$ , respectively.

**Table 1**  
Composition of dispersion and dry film in mass fractions.

	Dispersion $x/[-]$	Dry film $x/[-]$
Graphite (Hitachi)	43.5	91.7
Carbon black (C65)	1.4	2.8
Binder (PVDF)	2.6	5.5
Solvent (NMP)	52.5	—

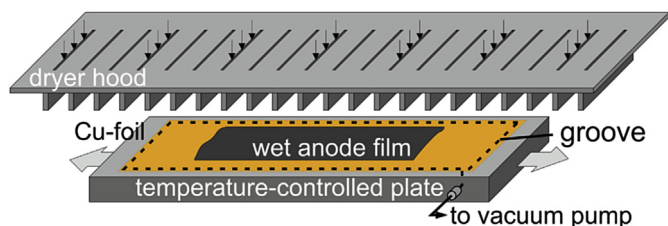


**Fig. 1.** Schematic of the experimental coating and drying set-up comprising a convective impingement dryer and a temperature-controlled plate introducing heat by contact.

### 2.3. Drying

Wet film application and transfer of the wet film into the dryer were carried out simultaneously in a single step with the elapsed time between coating and first dryer nozzle being less than a second. The dryer was designed following the recommendations for optimized impingement dryers given by Martin and Schlünder [35] and Polat [36]. Two feed blowers (Elektorr SD5-FU/FUK, Ostfildern, Germany) were operated at 100% and 25% of the maximum frequency for the high and the low drying rate, respectively. Transition from the first to the second blower was realized by a valve. To balance the non-uniform distribution of the heat and mass transfer coefficient imposed by the impingement dryer, the wet films were periodically moved below the dryer at a speed of  $100 \text{ mm s}^{-1}$ . This homogenization is a prerequisite to prevent undesired side-effects induced by local inhomogeneity in drying rate [13]. The experimental set-up allowed for almost isothermal drying conditions. Most notably the improved heat input provided by the temperature-controlled plate in combination with the evacuation of air between aluminum plate and copper foil by a vacuum pump allowed for almost constant film temperatures during drying, with a  $\Delta T$  resulting from evaporative cooling of less than 0.5 K for the drying conditions and materials applied. Further details are provided in the [supporting information](#).

### 2.4. Experimental approach

Throughout the experiments, the drying was conducted at either a low (LDR) or a high drying rate (HDR). Reference samples were produced both for LDR and HDR boundary conditions. Additional films were produced under systematic alteration of the drying rate after defined time intervals, starting at harsh drying conditions (HDR) and making a transition to LDR while the film is still loaded with solvent. [Fig. 2](#) schematically illustrates the experimental procedure.

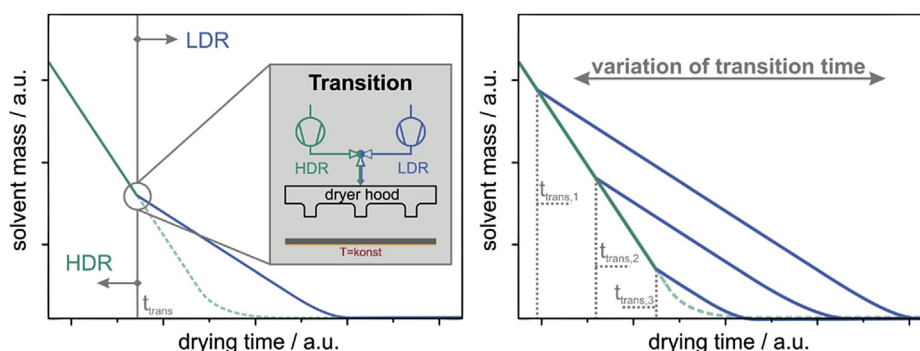


**Fig. 2.** Illustration of the experimental approach used within this work. *Left:* Each film is initially dried at a high drying rate (HDR). After a predefined drying time  $t_{\text{trans}}$  a transition is made to a low drying rate (LDR) by switching to a second blower running at a lower frequency. *Right:* For various transition times, films are produced.

The solvent mass decreases rapidly during the first drying stage at HDR. After a pre-defined time interval, the drying rate is abruptly decreased to LDR by switching to a second supply fan that is operated at a lower frequency. For various transition times, films were produced and subjected to characterization. The employed experimental approach is capable of revealing the time-resolved evolution of film properties such as the adhesive force or the binder concentration at the top or bottom surface on the basis of dry film characterization. This is achieved by the combination of two different drying rates whose influence on the underlying and property-determining processes, such as binder migration, significantly differs in magnitude. By increasing the transition time from high to low drying rate, the emphasis was gradually shifted towards processes promoted by the high drying rate and vice versa.

### 2.5. Drying kinetics

Drying curves were produced for investigation into the drying kinetics. Both coating and drying were executed as described before. However, the drying was stopped after a defined time interval and part of the film was scraped off. The weight of the samples was determined gravimetrically prior and subsequently to a second drying step conducted for 12 h at  $76.5^\circ\text{C}$  in a vacuum furnace. The solvent loading of the sample was calculated afterwards.

### 2.6. Adhesion

Prior to characterization, samples were stored in a vacuum furnace ( $p \approx 10 \text{ mbar}$ ) for 48 h at  $76.5^\circ\text{C}$ . Adhesion was measured by means of a  $90^\circ$  peel test. A universal testing machine (AMETEK LS1) was equipped with a  $90^\circ$  peel test device (AMETEK TH50). The electrode films were cut orthogonally to coating direction with a width of 30 mm. The samples were fixed on a metal sheet by double-sided adhesive tape with the graphite layer facing the tape. The whole stack was then pressed with a defined line load of  $2.8 \text{ kN m}^{-1}$ , sited on the slide of the  $90^\circ$  peel test device and fixed laterally with two metal bars. The uncoated, lateral part of the copper foil was fixed with a clamp, which was attached to a vertical traverse via a 10 N load cell. The traverse was then moved at a constant speed of  $50 \text{ mm min}^{-1}$ . The measuring signal of the load cell was logged by a computer. The  $90^\circ$  arrangement provokes an almost complete delamination of the active, porous graphite layer from the substrate. This characteristic constitutes a fundamental requirement for the experiments conducted in this work and the conclusions drawn as an outcome of this. Therefore, evidence is provided in the [supporting information](#) in the form of SEM micrographs of the copper foil after delamination and pore size

distributions measured by means of mercury intrusion porosimetry for LDR and HDR samples.

### 2.7. Detection of binder by EDS

The samples were qualitatively characterized by applying energy-dispersive x-ray spectroscopy (EDS; EDAX Apollo 40 SSD with Gemini 6 software, Mahwah, USA). Fluorine was used as tracing element for the presence of the PVDF binder. The amount of fluorine was detected at the surface of the electrode film and at the delaminated interface after peeling-off the current collector foil. Electron beam energies of 5 kV were chosen for the EDS measurements in order to shift the volume of interaction towards the particle surface where the binder is located. It has to be emphasized that, due to the sample heterogeneity, EDS is not perfectly suited to determine absolute concentrations of certain elements. However, observation of relative changes of the count rate under constant conditions has turned out to be a feasible method for gathering reliable information. For estimation of the standard deviation of the detected fluorine concentration, three measurements were conducted at the upper surface and the delaminated interface of a sample. The standard deviations were found to be 1.1% and 3.8%, respectively.

### 2.8. Electrochemical characterization

To assess the significance of drying process and binder migration on the electrochemical behavior, cell tests were carried out with graphite anodes dried at LDR and HDR. In order to obtain realistic testing conditions full-cells were built in pouch bag configuration. The electrode size was  $54 \times 54 \text{ mm}^2$  for the anode and  $50 \times 50 \text{ mm}^2$  for the cathode. For the preparation of the cathode  $\text{LiNi}_{0.33}\text{Mn}_{0.33}\text{Co}_{0.33}\text{O}_2$  (NMC; NM 3100, Toda Kogyo Corp.) was chosen as active material. The final composition of the dried cathodes was 87 wt% NMC, 5 wt% graphite (KS 6L, Imerys), 4 wt% carbon black (Super C65, Imerys) and 4 wt% PVdF (Solef 5130, Solvay). The dried sheets were compacted to a porosity of 40% for cathodes and 50% for anodes using a heated calendar (GKL 200, Saueressig) before cutting the electrodes. A commercial electrolyte (LP30, BASF) was used, containing 1 M  $\text{LiPF}_6$  in a 1:1 mixture of EC and DMC. Separion® (Litarion, Germany), a polymer foil containing ceramic particles, was used as separator. Prior to cell assembly, both electrodes and separators were dried overnight in a vacuum furnace at  $130^\circ\text{C}$ . Pouch cell assembly was conducted in a dry room ( $T_{\text{dew}} \leq -50^\circ\text{C}$ ).

The cycling tests were performed at  $23^\circ\text{C}$  between 3.0 V and 4.2 V in constant current mode (CC). At first, all cells were formatted by two 0.05C cycles. Following cycles were performed symmetrically at 0.5C, 1C, 2C and 3C, each step repeated 10 times. Afterwards the rates were lowered again to 0.5C (10 cycles) and 1C (20 cycles) to check on the recovery capability of cell capacity. Cycling voltage limits were set at 3.0 V and 4.2 V. The C-rate was calculated based on the theoretical capacity of the NMC cathode material ( $155 \text{ mAh g}^{-1}$  within full cells comprising graphite).

## 3. Results and discussion

### 3.1. Evolution of binder gradients during drying

Fig. 3 shows the adhesive force determined by  $90^\circ$  peel tests as a function of transition time from high to low drying rate.

The experimental transition times were defined based on the total time required for solvent to evaporate at sharp drying conditions ( $t_{\text{dry}} \approx 65 \text{ s}$ ). Beyond the samples that have been subjected to a change of the mass transfer while in the wet state, the adhesive

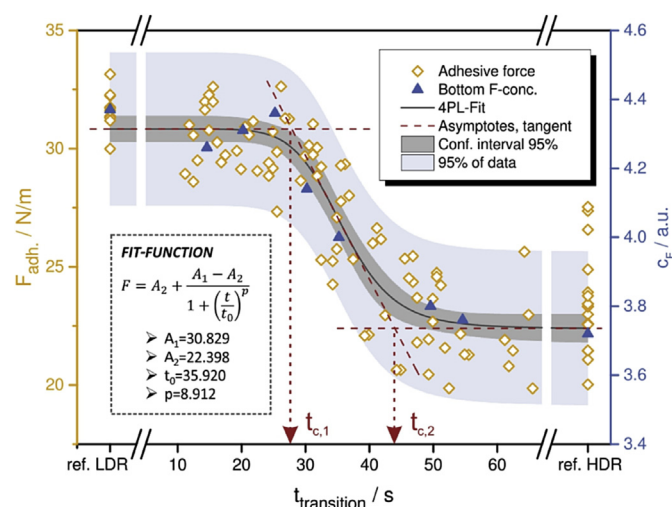


**Fig. 3.** Development of adhesive force and fluorine concentration at the delaminated surface over transition time compared to LDR and HDR reference samples. The adhesion of a sample initially subjected to HDR for 20 s and subsequently dried at LDR is therefore plotted at  $t_{\text{transition}} = 20 \text{ s}$ . Statistics are included based on a 4PL fit function. Characteristic transition times are estimated by intersecting asymptotes and a tangent drawn to the point of inflection.

force of reference samples has been included for both the high (HDR) and the low drying rate (LDR). The plot shows a broad distribution of the obtained transition times for the specimens. Due to the instant alteration of the drying rate in the entire drying chamber, film domains that have been coated and moved into the dryer first were exposed to the high drying rate for a longer time. The sample's accurate transition time therefore depends on its position on the temperature-controlled aluminum plate that carries the applied wet film into the drying chamber subsequent to film casting. For analysis of the experimental data a four parameter logistic (4PL) nonlinear regression function is given along with a 95% confidence interval and a forecast also including 95% of potential further measurements.

Based on the fit parameters, an average adhesive force of  $F_{\text{max}} = 30.8 \text{ N m}^{-1}$  was found for LDR, while HDR resulted in considerably lower values of  $F_{\text{min}} = 22.4 \text{ N m}^{-1}$ . Despite the mean variation, all measured adhesive force values fall within the range confined by the reference samples. The increase in drying rate induced by higher mass transfer coefficients resulted in a pronounced decrease in adhesive force of about 30%. For transition times that fall below a first characteristic transition time of  $t_{c,1} = 28 \text{ s}$ , a constant adhesive force is observed equal to that of the LDR-reference sample. A second level of constant adhesion exists for transition times exceeding a second characteristic transition time of  $t_{c,2} = 44 \text{ s}$ . The characteristic times were approximated by the intersection of the confining asymptotes and a straight, tangential line drawn to the point of inflection that exists in the intermediate drying section and presents the instant of greatest reduction in adhesive force. In the intermediate time interval, the course of the adhesive force is characterized by a sharp drop from LDR to HDR adhesion level. The evolution of the structure of the substrate-near film domains which is most likely to be responsible for the variation in the magnitude of the adhesive force of the dry film can therefore be segmented into a tripartite process.

Fig. 3 evidences the existence of a characteristic drying period featuring a distinct sensitivity regarding the adhesive force.  $90^\circ$  peel tests promote a delamination of the active layer at the interface between current collecting copper foil and porous graphite layer with only residual amounts of solid sticking to the copper foil.



Therefore, the discovery of the tripartite nature of this process is on this basis not applicable to other film properties, yet. To provide a solid foundation for interpretation of the processes governing the magnitude of the adhesive force, a link to a micro-structure relevant parameter is crucial. This relation is established in the following. The film's mechanical integrity is provided by the polymeric binder that is incorporated into the dispersion in small amounts. Both cohesion (attachment of connecting particles) and adhesion (attachment of the porous film to the substrate) are most presumably related to the distribution and the amount of binder in the interstices of the film and at the interface with the substrate. In the specific case of an adhesive failure at the interface between substrate and active layer, the binder concentration in the delamination plane is of great interest. To critically review the hypothesis of a dependence of adhesive force and binder concentration in the delamination plane, PVDF concentration was determined by detection of fluorine by means of energy-dispersive x-ray spectroscopy (EDS) and compared to the course of the adhesive force.

It is obvious, that both adhesive force and detected fluorine develop proportionally. This strengthens the evident interpretation of a direct interrelation of adhesive force and binder concentration in the delamination plane at the substrate interface. The fluorine concentration is determined as relative amount of atoms detected at the surface. The absolute values strongly depend on the measuring parameters and therefore just allow for qualitative interpretation. The predominant effect is the limited penetration depth of EDS measurements. Fluorine is therefore detected in disproportionately high amounts compared to graphite.

It is well known from literature that the adhesive force of electrode films is strongly related to the drying conditions applied during solvent removal [11,12,37]. In a previous publication [11] by the authors that also employed an isothermal drying routine, the correlation of drying rate and adhesive force was discussed. A decrease in drying rate adjusted by variation of the drying temperature was found to improve adhesive force. In a non-isothermal process, Westphal et al. [12] observed analogous trends of decreasing adhesive force for increasing drying rates. These findings are further strengthened by the results discussed above. They, however, contradict the results given by Despotopoulou and Burchill [37]. They found an optimized adhesive force at drying temperatures of 155 °C. For lower and higher drying temperatures, the adhesive force decreased. Due to the high drying temperatures applied and the long drying times adjusted, an annealing effect might superpose the actual drying effect on the adhesive force though. In addition, the viscosity of the slurry applied was considerably low eventually permitting sedimentation.

Fig. 4a shows the superposition of an SEM micrograph and the corresponding fluorine mapping of the surface of a graphite layer. The picture discloses the close affinity of binder and carbon black. This observation is interpreted later on in Section 3.3.3. However, it has to be stated that fluorine is not detected at every expected site (e.g. marked area in Fig. 4a). The take-off angle for the EDS detector is 34°; so, rough surfaces always experience shadowing of some areas. To allow for comparison of various samples, the impact of surficial domains not captured by EDS has to be minimized. This is done by relative quantification: as carbon is subject to the same shadowing effect as fluorine relating the fluorine content to the carbon content results are normalized and different samples become comparable. Furthermore relatively large areas of about 1 mm<sup>2</sup> are inspected for quantification which broadens the statistical basis. Exemplary EDS spectra are provided in Fig. 4b for a LDR and a HDR reference sample. The spectra exhibit three distinguished peaks with different characteristic energies. The most pronounced peak represents carbon (~0.3 keV), which is the predominant component. Both the oxygen (~0.5 keV) and the fluorine

peak (~0.7 keV) are considerably smaller.

In the previous section, adhesive force was correlated with the binder concentration in the vicinity of the substrate interface as a function of transition time. Although Fig. 3 allows for identification of a characteristic drying stage thereby granting first superficial insights into the drying process, it lacks information on the film solidification at particular instants during solvent removal. Conversion of the characteristic transition times into a volumetric quantity would provide a more illustrative picture of the film state at the moment the drying rate is changed. The required correlation is disclosed in Fig. 5 where the liquid to solid mass ratio is plotted over drying time for HDR boundary conditions.

The curve shows a distinct linear decrease of solvent content throughout almost the entire drying, a characteristic feature of the first drying stage often referred to as “constant rate period” (CRP) [38]. During CRP, the evaporation rate practically equals the evaporation rate of the pure solvent [39]. The CRP is often considered to continue as long as a closed liquid layer exists at the evaporating surface. Several authors however contradict this hypothesis and provide evidence for the CRP to endure even beyond the state of a saturated pore network.

A stagnant boundary layer at the film surface allows for the film to maintain a constant evaporation flux even when small dry patches exist [39,40]. The dry film porosity represents a suitable benchmark, since it not only provides a measure for the void fraction of the dry film, but also describes the volume fraction of solvent at the moment the final porous body is formed by the solid components and film shrinkage terminates. Strictly speaking, this is just true as long as the pores remain filled while the film is still shrinking. Furthermore, solvent absorption by graphite, carbon black or binder must be irrelevant. Considering the distinct constant rate period and the fact that PVDF is solved NMP, this assumption is justifiable. Redistribution of the solid active material particles is suppressed from this moment on due to steric hindrance. For the dry anode film a porosity of  $\epsilon = 0.59$  was determined by measurements of the dry film thickness and calculations following Equation (1):

$$\epsilon = 1 - \frac{M_s}{\bar{\rho}_s \cdot 10^{-3} \cdot d_{\text{film}}} \quad (1)$$

$M_s$  represents the area weight of the dry film in g m<sup>-2</sup>,  $\bar{\rho}_s$  is the average density of solids in kg m<sup>-3</sup> and  $d_{\text{film}}$  represents the dry film thickness in  $\mu\text{m}$ . The porosity equals a liquid to solid mass ratio of  $X = 0.65$ . This demonstrates the existence of an unchanged drying rate beyond the point when film shrinkage is completed and the liquid phase starts to recede into the porous structure.

Despite the linear decrease of solvent content with drying time, it can be seen that the initial solvent content does not comply with the linear regression. This certainly affects neither the linear character of the curve nor the drying kinetics itself, as the initial solvent content has been excluded from the data set for linear regression fitting. Nevertheless, the reasons should be briefly mentioned at this point. The drying times plotted on the X-axis represent the total drying time inside the dryer at high drying rate. The film however remains on the temperature-controlled aluminum carrier for an additional two to three seconds after exiting the dryer. While the film temperature is constant, the gas-side mass transfer coefficient and therefore the drying rate diminish abruptly to a significantly lower value. The actual decrease in solvent content before the film is scraped off the substrate, put in a dish and analyzed gravimetrically is therefore underestimated. A second contribution might be made by an incomplete removal of the film. Thin solvent films still present on the substrate can alter the average solvent content of the film that has been scraped off. Table 2 gives an

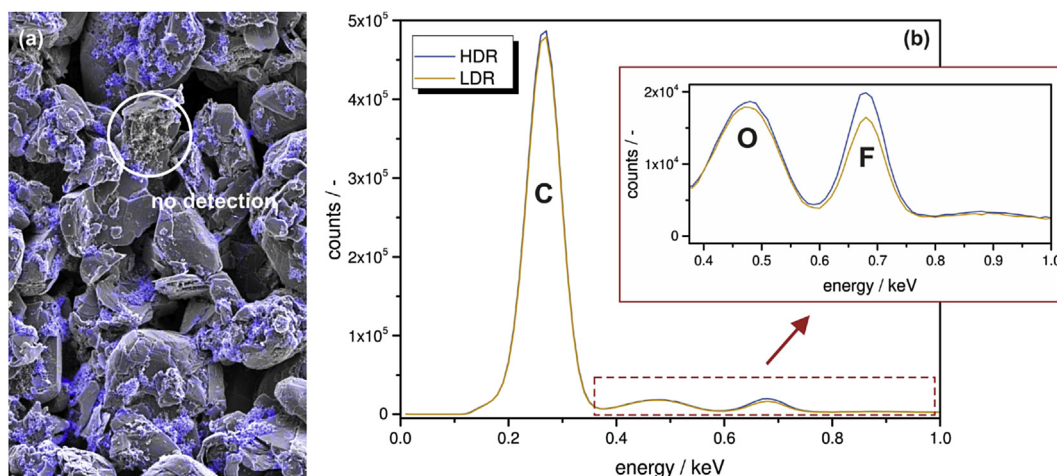


**Fig. 4.** (a) Superposition of SEM micrograph and fluorine mapping (blue color). (b) EDS spectra are shown for LDR and HDR reference sample. Three well-distinguished peaks (Carbon – C, Oxygen – O and Fluorine – F) can be detected. (For interpretation of the references to colour in this figure legend, the reader is referred to the web version of this article.)

overview of the two adjusted drying rates. The drying rates were calculated according to Equation (2) with  $X$  being the liquid to solid mass ratio and  $t$  being the drying time.

$$\dot{m}_{NMP} = \left. \frac{dX}{dt} \right|_{CRP} \cdot M_S \quad (2)$$

Additional information on the drying kinetics experiments is provided in the [supporting information](#).

The information on drying kinetics and drying rate can be utilized to convert the characteristic transition times  $t_{c,1}$  and  $t_{c,2}$  into characteristic solvent volume fractions. The values were derived from the liquid to solid mass ratio that can be described as a function of transition time based on the results shown in Fig. 5. The calculated solvent volume fractions were  $\phi_{NMP, c1}^{transition} = 0.584$  and  $\phi_{NMP, c2}^{transition} = 0.442$ . Considering the fact of the tangent method generally intersecting at too low volume fractions, we can conclude that the value of the dry film porosity approximately equals the first characteristic solvent volume fraction.

Fig. 3 shows a decrease in binder concentration at the substrate

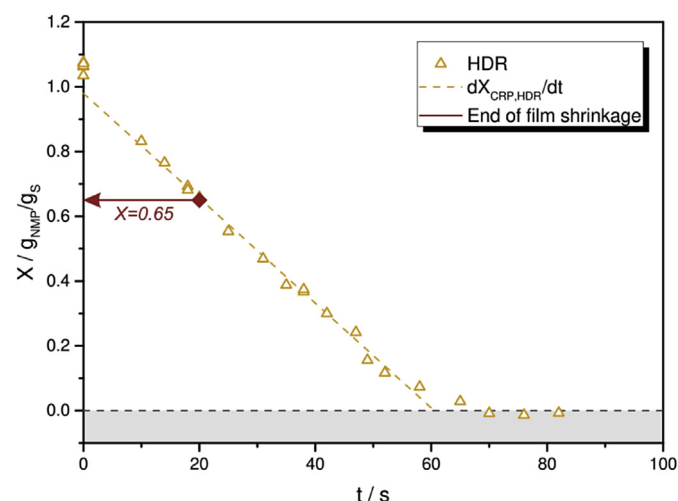


**Fig. 5.** Drying curve for high drying rate (HDR). The linear trend shows that the drying process is describable by a constant evaporation rate (dashed/dotted line), which is characteristic for the “constant rate period” (CRP).

interface with increasing transition time. This depletion must necessarily be accompanied by the enrichment of binder elsewhere in the film. EDS as applied on delaminated films was also used for fluorine detection at the specimen's surfaces. Fig. 6 opposes the top and bottom fluorine concentration. Two representative SEM micrographs for the surface and the delaminated interface illustrate the different nature of the topographies that hinder a quantitative comparison of the top and bottom binder concentration. The ordinate values are therefore provided as arbitrary units. The qualitative interpretation of the curves is, however, of great interest. While binder concentration at the bottom and degradation of adhesive force both display a distinct plateau for short transition times (Figs. 3 and 6), the binder concentration at the top surface increases from the very beginning before reaching a constant level. For both the top and bottom binder concentration a constant level is found for transition times exceeding the second characteristic transition time. Although the film is still in a partially wet state, the binder seems to immobilize over the entire film height after a critical state during film solidification.

### 3.2. Impact on electrochemical properties

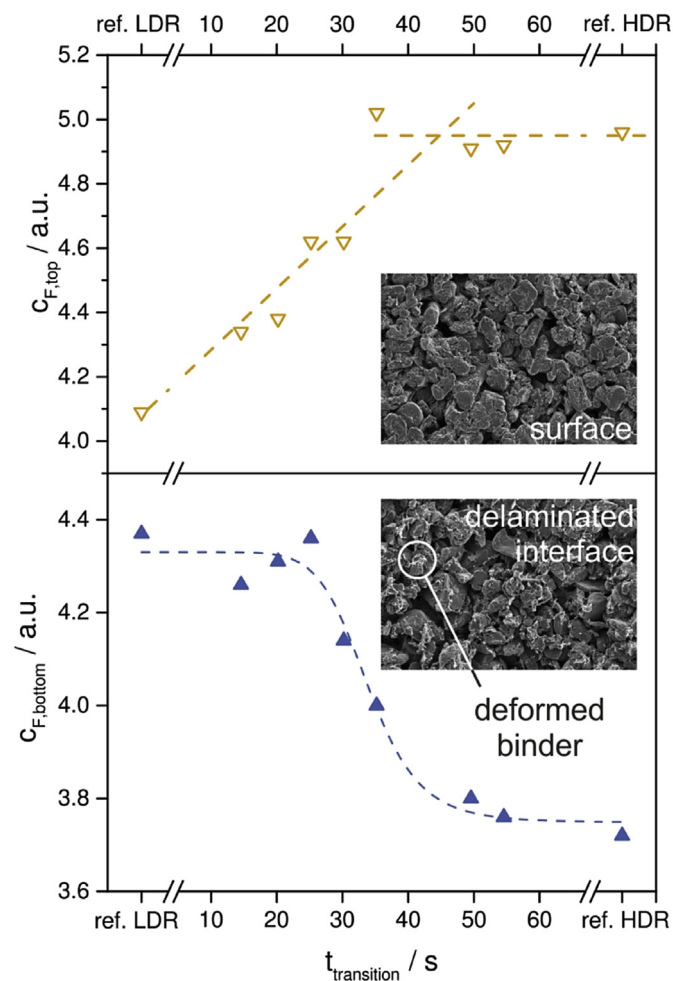
Fig. 7 shows galvanostatic charge and discharge profiles of full cells based on HDR and LDR reference samples between the cutoff voltages of 3.0 V and 4.2 V.

For three different C-rates, the second, the fifth and the tenth cycle are displayed. The profiles represent the superposition of cathode and anode based effects. Nevertheless, the impact of a high drying rate on the anode properties is clearly observable, since cathodes were produced under standardized conditions. All samples processed at HDR show an additional loss of capacity which primarily results from incomplete charging due to a high overpotential caused by charge transfer limitations arising at the anode.

**Table 2**  
Adjusted parameters for high (HDR) and low drying rate (LDR).

	High drying rate (HDR)	Low drying rate (LDR)
$T_{iso}/^{\circ}C$	76.5 $^{\circ}C$	76.5 $^{\circ}C$
$f/f_{max}/\%$	100	25
$\dot{m}/g/(m^2 s^{-1})$	1.19	0.52

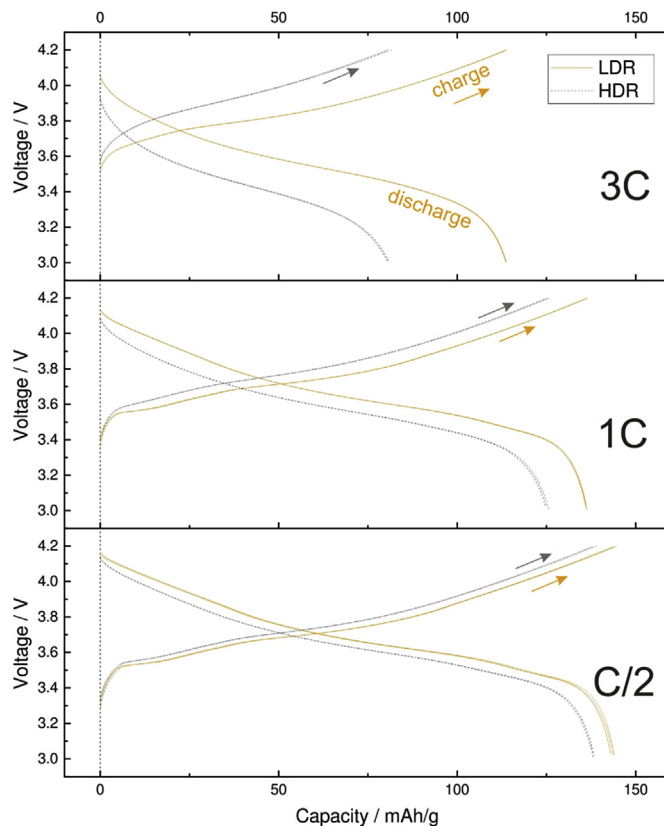
$f/f_{max}$  represents the relative frequency of the fan.  
 $\dot{m}$  is the evaporation rate of NMP.



**Fig. 6.** Top and bottom binder concentration determined by EDS over transition time and for HDR and LDR reference samples. The SEM micrographs show the (smooth) surface (top) and the delaminated interface (bottom) exhibiting binder structures that have been deformed by the delamination process.

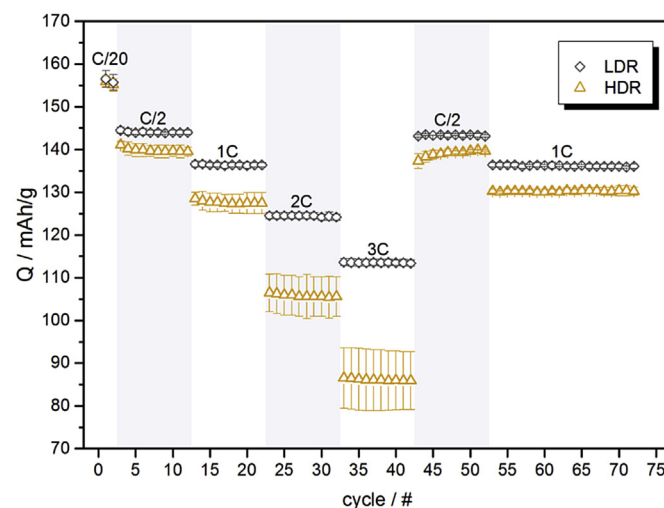
This difference can be attributed to several effects. As disclosed in Fig. 6, binder accumulation at the electrode surface takes place at high drying rates. Additionally, binder depletes at the interface between active graphite layer and substrate. One explanation for the decrease in charging capacity could be an aggravated intercalation of lithium ions in the particles or parts of aggregates that are located in the vicinity of the anode surface due to an augmentation of polymer layers prohibiting contact between electrolyte and graphite. Beyond, carbon black could be a relevant factor as well. Fig. 4a indicates a close affinity of binder and carbon black. It is therefore likely that both binder and carbon black tend to accumulate at the surface and to deplete at the buried interface. Literature supports this hypothesis, since migration of small particles was reported on before [7,8,23]. This migration could attribute to an inferior conductivity in the case of harshly dried anodes in film domains located in the vicinity of the current collector. Wang et al. [41] disclose the superior role of conductive paths regarding cell performance, especially when relatively large active material particles are used that provide a rather small number of contact points between the particles.

Fig. 8 shows the entire rate capability test, underlining the conclusions drawn from Fig. 8. Both for 0.5C and 1C the capacity obtained from cells after cycling at high C-rates is identical to the capacity of cells before. The capacity loss at this point is therefore



**Fig. 7.** Charge/discharge profiles of cells based on LDR and HDR reference anodes for 0.5C, 1C and 3C. Shown are cycles 2, 5 and 10 for each C-rate. Capacity refers to NMC mass.

reversible and not rooted in cell degradation but rather in an increase in reversible charge transfer limitations. Although the adhesion of the HDR anode is reduced, it still seems to be high enough to prevent immediate delamination of the electrode layer. Nevertheless, it cannot be excluded that distinct aging can take place due the weakened interface for higher cycling numbers, which would further amplify the role of the drying process.



**Fig. 8.** Rate capability of cells based on HDR and LDR reference anodes. Capacity refers to NMC mass.

### 3.3. Film solidification model

The most important mechanistic findings disclosed in this paper are summarized in the following, assessed on the basis of the state of knowledge and incorporated in a mechanistic model describing film solidification.

1. The drying of the anode system subjected to investigation was found to be predominantly controlled by mass transport in the gas-phase. Therefore a distinct constant rate period prevails at least down to low liquid to solid mass ratios of less than 10%, but most likely for even longer.
2. The adhesive force obtained from 90° peel tests was found to strongly relate to the PVDF concentration in the delamination plane. For increasing drying times at HDR, the binder concentration decreases at the interface between substrate and active layer.
3. The film's final adhesive force and consequently the binder concentration at the bottom evolve in a characteristic, well-defined time interval. Distinct levels of constant adhesion were found for transition times/solvent volume fractions falling below a characteristic value  $t_{c,1}/\phi_{c,1}$  or exceeding a second characteristic value  $t_{c,2}/\phi_{c,2}$ .
4. Binder enriches at the top surface of the film preferentially under harsh drying conditions. This accumulation seems to be taking place from the very beginning of the drying process. Similarly to the bottom PVDF concentration, a level of constant concentration is available for transition times exceeding  $t_{c,2}$ .

The enrichment of binder at the top surface and its depletion at the bottom strongly points towards a mechanism often referred to as binder migration [2,6–8,23,29,31,33]. Li and Wang [7] investigated the binder distribution of water and organic based binder systems in a LiCoO<sub>2</sub> electrode by means of thermogravimetric analysis of thin layers abraded by a knife. For both binder systems a gradient of increasing binder concentration towards the film surface was discovered. Binder migration therefore occurs both for soluble and particulate binder, the distribution being less uniform for the organic PVDF binder. To allow for sufficiently large sample quantities, electrodes with a dry film thickness of about 1500 µm were produced. The authors attributed the binder migration to the solvent flow towards the surface due to capillary action during the constant rate period. The drying kinetics obtained for the thick films, however, shows a significantly different trend of a pronounced falling rate period compared to the one obtained in this work. This most probably is rooted in lateral drying phenomena like lateral drying fronts or the considerably large film thickness impressing a diffusive limitation throughout the porous film due to tortuosity [38]. The underlying processes are therefore not adoptable to thin films without making any restrictions.

While Li and Wang [7] determined the binder distribution on the basis of dry electrodes, Lim et al. [8] made first experiments on real-time observation of binder migration by means of fluorescence microscopy on dilute and carbon-black-free graphite dispersions featuring considerably high binder concentrations. Generally, the fluorescent polystyrene particles were again found to migrate towards the surface due to capillary driven forces. The extent of capillary action was found to be a function of CMC concentration and the degree of the evolution of a consolidation layer during drying. No accumulation of binder was observed in the initial drying regime. This opposes this work's findings presented in Fig. 6. They applied highly dilute dispersions, whereas dispersions with a solid content of almost 50% were subjected to research within this work, though. The required time for the evolution of a consolidation layer, both on an absolute and relative basis, is therefore longer

for the dilute system. In contrast, formation of a consolidation layer is expected to happen very early in our experiments. They also suggest the change in refractive index due to particle enrichment in the upper region to account for a decrease in fluorescence. The results are therefore not necessarily contradictory. Our comparison of binder concentration evolution at the free surface and the substrate interface suggests a top-down consolidation mechanism further reinforcing the assumption of a gradual film consolidation by Lim et al. [8].

Hagiwara et al. [23] introduced Raman spectroscopy as suitable experimental technique towards research on binder distribution in battery coatings. Graphite films were produced with high SBR binder concentrations and immersed into liquid nitrogen after defined drying times. After a freeze drying step, cross sections were investigated regarding the SBR concentration profile in the electrode. Drying under ambient conditions resulted in uniform binder distributions, whereas sharp drying conditions promoted binder migration towards the free surface. This matches our finding of stronger binder segregation over film height for higher drying rates. Hagiwara et al. found migration to last longer in lower film domains, which might be attributed to a steric hindrance due to highly filled pores in the upper layer (keep in mind the high binder content) or the receding drying front. Their results suggest the existence of an overall starting time for binder migration to initiate. However, time intervals between sampling are rather large, the precise moment of initiation, therefore may be slightly different to that shown.

Publications on binder migration in drying battery electrode films are scarce, further research is therefore endorsed. Drawing a more detailed picture of the formation of the film microstructure obligates the fundamental understanding of characteristic drying stages or intermediate wet film states during drying. The time of appearance of binder migration is a complex function of a multitude of influencing factors. The most fundamental processes are evaporation, diffusion and sedimentation [14,42,43]. Depending on the anode slurry and film properties and the drying boundary conditions either one process dominates, or a complex interplay of two or even all three processes prevails. Each of them is again a function of further parameters. The evolution of a diffusive limitation inside the film is for example conceivable especially for thick films and would affect the evaporation rate and therefore the balance between the three processes mentioned. Sedimentation can slow down due to an increase in viscosity accompanied with solvent removal. Without further information, comparison of various results is therefore highly aggravated.

Luo et al. [6] provided a solidification mechanism for silica coatings containing a latex binder. It is based on the fundamental solidification mechanism of latex dispersions [27,44]. A few major differences compared to the material system used in this work have to be kept in mind:

- Latex dispersions often feature unimodal or at least narrow particle size distributions. Pore radius distributions therefore differ strongly from the pore structures obtained from graphite powders with a broad particle size distribution. This is further aggravated by the addition of carbon black nanoparticles.
- The majority of publications on latex dispersions apply particulate binders, whereas a soluble binder was employed in this work.
- Latex binders featuring a low glass transition temperature tend to coagulate and interdiffuse later on during drying, thereby forming a compact film. The coagulation step does not occur for hard particles, for which reason a porous film is formed in this case.



Based on the findings disclosed in this work and the work previously published by other authors in literature, a mechanism describing film solidification is proposed in the following.

### 3.3.1. Top-down consolidation

NMP evaporation initiates at the gas/liquid interface and induces a decrease in solvent concentration in the surface-near film domains thereby increasing the particle and polymer concentration. Without sedimentation, the large graphite particles in the first instance roughly hold their initial position. As soon as the free liquid surface recedes into the interstices of the first particle layer, menisci are formed and capillary forces start to evolve [6,29,44]. Due to the high initial volumetric solid content of the slurry applied within this work, the evolution of first, weak capillary forces would be expected to appear early during drying. Lateral attraction further reinforces the particle clustering [45] as possibly does depletion flocculation [46]. The phenomenon of cluster formation at the evaporating surface is referred to as “top-down” consolidation in literature [6,44]. Below the menisci, the pressure lowers and the pressure gradient takes effect on the particles that pin the liquid menisci by pulling them downwards into the bulk of the film to compensate for solvent evaporation. The particles being pulled down displace the local liquid phase, forcing it to evade laterally and move upwards. The thicker the consolidation layer, the higher the share of displaced bulk-liquid. The capillary force thus introduces a relative movement between the continuous, liquid phase and the active material particles, which represents a prerequisite for the evolution of a PVDF gradient throughout the film. Although the pressure gradient is capable of transporting the liquid phase through the consolidated structure towards the evaporating surface, it does not attract particles from below the consolidation layer. Growth of the consolidation front is solely caused by film shrinkage and collection of particles underway [6]. This is in good agreement with the early increase in PVDF concentration at the surface and the constant concentration at the bottom (Fig. 6). Although not being observable in the results, a very short plateau of the free surface binder concentration would be expected at the very beginning of the drying process due to the absence of capillary forces before first menisci evolve.

### 3.3.2. Diffusion

A second mechanism is required for explanation of the binder gradient's dependency on drying rate. Diffusion was derived as potentially decisive mechanism from theoretical considerations [29]. Baunach et al. [11] implemented diffusion into the film consolidation model proposed by Luo et al. [6] and applied it to a Lithium-ion battery electrode film. Although a material system comprising a latex binder was investigated in Luo's work, the fundamental processes are most likely comparable, since pore structure, viscosity and initial solvent content were similar. The accumulation of binder in the consolidation layer produces a concentration gradient triggering back diffusion directed towards the substrate. The total drying time and therefore the time available for diffusion is defined by the drying rate. For low drying rates, sufficient time is available for the balancing of the concentration gradient. On the contrary, binder will pile up near the surface for high drying rates. Back diffusion is also influenced by the molecular size of the binder. High molecular weight polymers exhibit lower diffusion rates and are therefore much more susceptible to accumulation at the surface, since back diffusion is slowed down.

### 3.3.3. Drying of the consolidated layer

Consolidation layer growth sustains until it reaches the substrate and forms the final porous body. Film shrinkage terminates at this point. Ideally, the pore structure is saturated with liquid at this

point and the solvent volume fraction equals the dry film porosity as observed in the experiments presented. Due to the heterogeneous pore structure of the film it is however likely, that individual pores start to empty, before the consolidation is entirely completed, especially for high drying rates. Large pores will empty first due to the difference in capillary pressure [29]. As soon as the large pores start to empty, convective flow can transport the liquid phase. Further solvent removal forces the gas/liquid interface to recede into the bulk. As a consequence, wet patches are very likely to be still available at the surface after air already started to infiltrate the film. This has previously been observed for drying latex systems [47]. Agglomerates of carbon black form the smallest pores which dry at last. This is one reason for binder being predominantly found in the interstices between particles and especially in the vicinity of carbon black (Fig. 4a). This implies in the first place that wet clusters can exist even in regions close to the film's surface for a long time during drying. The shape of the receding drying front therefore necessarily depends on the local pore structure and progresses both vertically and horizontally. While an interconnected liquid network persists throughout the porous structure at the moment film shrinkage stops, only small liquid clusters will be available at a certain point later on during drying, thereby eliminating global capillary transport. This is – at this point – assumed to be the most probable reason determining the appearance of the second characteristic point in Figs. 3 and 6. Immobilization due to narrow pore dimensions and steric hindrance [48] would be expected at an earlier point during drying and can be neglected both for soluble binders and the carbon black nanoparticles. The immobilization mechanism is however subject to ongoing research.

## 4. Conclusion

A new experimental approach was disclosed providing a way to investigate the time-resolved evolution of significant film properties of a drying anode film. Both energy-dispersive x-ray spectroscopy and 90° peel tests were employed to investigate the film's adhesive force on a copper substrate and the binder concentration at the free surface and the delaminated interface.

The evolution of the adhesive force was found to be tripartite. A characteristic intermediate stage sensitive to high drying rates is confined by two stages of constant adhesive force. The adhesive force was demonstrated being a function of the binder concentration in the delamination plane, i.e. the interface between substrate and porous graphite layer. The adhesive force therefore represents an easy accessible, indirect measure for the binder concentration in the delamination plane. The development of binder concentration at the surface exhibited a completely different nature. The initial level of constant binder concentration prevailing at the bottom was not observed at the surface. In fact, the binder concentration increased from the very beginning of the drying process before reaching a constant level.

The findings strongly support the presence of a top-down film consolidation. A consolidation layer quickly evolves at the evaporating surface in the absence of sedimentation and for comparably high solid contents of the slurry. Capillary action and film consolidation promote the enrichment of binder in the vicinity of the menisci thereby forming a gradient throughout the film. As the consolidation layer grows due to solvent evaporation, the area of influence expands until it approaches the substrate. Binder migration was found to continue beyond the point at which shrinkage terminates. If sufficient time is available the resulting binder gradients can equilibrate because of back diffusion, but with high drying rates the binder will accumulate preferably at the surface and within the film. The inhomogeneous binder distribution in the anode introduced by HDR provokes inferior rate

capability and a decrease in cell capacity. An optimization of the drying process and an acceleration of the drying speed are therefore merely feasible if drying conditions are applied that preserve an appropriate binder distribution. The present study offers assistance to this task as it localizes the characteristic drying stage governing binder movement and concentration. Nevertheless, the impact of a multitude of relevant parameters such as drying rate, film composition, type of binder, particle size distributions is still insufficiently understood and therefore subject of ongoing research.

## Acknowledgements

This work was funded by the German Research Foundation (DFG, grant SCHA 1266/9-1) and the Federal Ministry for Economic Affairs and Energy (BMW, 03ET6016). The authors would like to thank “Project Competence E” at KIT for the cooperation and the students involved in this work: R. Govindarajan, N. Sanchez Salach and M. Mussler.

## Appendix A. Supplementary data

Supplementary data related to this article can be found at <http://dx.doi.org/10.1016/j.jpowsour.2016.04.018>.

## References

- [1] P.C. Norrdahl, Tappi J. 74 (5) (1991) 73–78.
- [2] G. Engström, M. Rigdahl, J. Kline, J. Ahlroos, Tappi J. 74 (5) (1991) 171–179.
- [3] J.E. Kline, Tappi J. 74 (4) (1991) 177–182.
- [4] A.K. Atmuri, S.R. Bhatia, A.F. Routh, Langmuir 28 (2012) 2652–2658.
- [5] R.E. Trueman, E. Lago Domingues, S.N. Emmett, M.W. Murray, J.L. Keddie, A.F. Routh, Langmuir 28 (2012) 3420–3428.
- [6] H. Luo, C. Cardinal, L.E. Scriven, L.F. Francis, Langmuir 24 (2008) 5552–5561.
- [7] C.-C. Li, Y.-W. Wang, J. Electrochem. Soc. 158 (2011) A1361–A1370.
- [8] S. Lim, K.H. Ahn, M. Yamamura, Langmuir 29 (2013) 8233–8244.
- [9] P.G. Bruce, B. Scrosati, J.-M. Tarascon, Angew. Chem. Int. Ed. 47 (2008) 2930–2946.
- [10] B. Lestriez, C. R. Chim. 13 (2010) 1341–1350.
- [11] M. Baunach, S. Jaiser, S. Schmelzle, H. Nirschl, P. Scharfer, W. Schabel, Dry. Technol.: Int. J. 34 (4) (2016) 462–473.
- [12] B. Westphal, H. Bockholt, T. Günther, W. Haselrieder, A. Kwade, ECS Trans. 64 (2015) 57–68.
- [13] D.J. Harris, J.A. Lewis, Langmuir 24 (2008) 3681–3685.
- [14] A.F. Routh, W.B. Russel, AIChE J. 44 (1998) 2088–2098.
- [15] R. Dominko, M. Gaberscek, J. Drofenik, M. Bele, S. Pejovnik, J. Jamnik, J. Power Sources 119–121 (2003) 770–773.
- [16] G.-W. Lee, J.H. Ryu, W. Han, K.H. Ahn, S.M. Oh, J. Power Sources 195 (2010) 6049–6054.
- [17] H. Zheng, L. Zhang, G. Liu, X. Song, V.S. Battaglia, J. Power Sources 217 (2012) 530–537.
- [18] H. Bockholt, W. Haselrieder, A. Kwade, ECS Trans. 50 (2013) 25–35.
- [19] V. Wenzel, R.S. Moeller, H. Nirschl, Energy Technol. Wein. Ger. 2 (2014) 176–182.
- [20] W. Haselrieder, S. Ivanov, H.Y. Tran, S. Theil, L. Froböse, B. Westphal, M. Wohlfahrt-Mehrens, A. Kwade, Prog. Solid State Chem. 42 (4) (December 2014) 157–174.
- [21] M. Schmitt, M. Baunach, L. Wengeler, K. Peters, P. Junges, P. Scharfer, W. Schabel, Chem. Eng. Process 68 (2013) 32–37.
- [22] M. Schmitt, P. Scharfer, W. Schabel, J. Coat. Technol. Res. 11 (2014) 57–63.
- [23] H. Hagiwara, W.J. Suszynski, L.F. Francis, J. Coat. Technol. Res. 11 (2014) 11–17.
- [24] Y.-H. Chen, C.-W. Wang, X. Zhang, A.M. Sastry, J. Power Sources 195 (2010) 2851–2862.
- [25] W. Haselrieder, S. Ivanov, D.K. Christen, H. Bockholt, A. Kwade, ECS Trans. 50 (2013) 59–70.
- [26] J. Kaiser, V. Wenzel, H. Nirschl, B. Bitsch, N. Willenbacher, M. Baunach, M. Schmitt, S. Jaiser, P. Scharfer, W. Schabel, Chem. Ing. Technol. 86 (2014) 695–706.
- [27] J.W. Vanderhoff, Br. Polym. J. 2 (1970) 161–173.
- [28] J. Watanabe, P. Lepoutre, J. Appl. Polym. Sci. 27 (1982) 4207–4219.
- [29] K.G. Hagen, Tappi J. 69 (1986) 93–96.
- [30] P. Lepoutre, Prog. Org. Coat. 17 (1989) 89–106.
- [31] A.E. Ranger, Pap. Technol. Bury, U. K. 35 (1994) 40–46.
- [32] Y.H. Zang, Z. Liu, Z.L. Cao, P. Mangin, J. Pulp Pap. Sci. 36 (2010) 79–84.
- [33] Y.-H. Zang, J. Du, Y. Du, Z. Wu, S. Cheng, Y. Liu, Langmuir 26 (2010) 18331–18339.
- [34] K. Terashita, K. Miyanami, Adv. Powder Technol. 13 (2002) 201–214.
- [35] H. Martin, E.U. Schuender, Chem. Ing. Technol. 45 (1973) 290–294.
- [36] S. Polat, Dry. Technol. 11 (1993) 1147–1176.
- [37] M. Despotopoulou, M.T. Burchill, Prog. Org. Coat. 45 (2002) 119–126.
- [38] G.W. Scherer, J. Am. Ceram. Soc. 73 (1990) 3–14.
- [39] M. Suzuki, S. Maede, J. Chem. Eng. Jpn. 1 (1968) 26–31.
- [40] E.-U. Schluender, Chem. Ing. Technol. 60 (1988) 117–120.
- [41] H. Wang, T. Umeno, K. Mizuma, M. Yoshio, J. Power Sources 175 (2008) 886–890.
- [42] C.M. Cardinal, Y.D. Jung, K.H. Ahn, L.F. Francis, AIChE J. 56 (2010) 2769–2780.
- [43] F. Buss, C.C. Roberts, K.S. Crawford, K. Peters, L.F. Francis, J. Colloid Interface Sci. 359 (2011) 112–120.
- [44] Y. Ma, H.T. Davis, L.E. Scriven, Prog. Org. Coat. 52 (2005) 46–62.
- [45] D. Stamou, C. Duschl, D. Johannsmann, Phys. Rev. E Stat. Phys. Plasmas Fluids Relat. Interdiscip. Top. 62 (2000) 5263–5272.
- [46] J.E. Seebergh, J.C. Berg, Langmuir 10 (1994) 454–463.
- [47] C.M. Cardinal, L.F. Francis, L.E. Scriven, J. Coat. Technol. Res. 6 (2009) 457–469.
- [48] K.G. Hagen, Tappi J. 72 (1989) 77–83.